New Insight Into Crack-Healing Mechanism *via* Electropulsing Treatment

QING CAI, MIAN ZHOU, EBAD BAGHERPOUR, SEYEDMEHDI HOSSEINI, CHAMINI MENDIS, ISAAC CHANG, and HAMID ASSADI

A combination of experiment and numerical simulation was employed to study the healing mechanism of fatigue crack *via* a novel route of electropulsing treatment (EPT) named dual-step EPT processing. By applying cyclic loads, similar cracks were generated in 316L stainless steel samples. Then, cracked specimens were subjected to electropulsing treatment under different conditions in order to find the optimum EPT condition to effectively heal the crack. The geometry of the fatigue crack before and after EPT was investigated in 3D by Micro-CT. SEM-EBSD was used to evaluate the microstructure of the healed region. To understand the dominant mechanism of crack healing by EPT, the temperature and stress/strain fields were evaluated by the finite element method (FEM) considering non-uniform Joule heating. The results demonstrate that complete crack healing requires a balanced combination of melting and compressive stress as well as increased peak current density regarding the reduced crack length. The simulations also suggest that Joule heating alone is sufficient to induce the observed melting in the examined samples. The fatigue crack after EPT was found to be effectively healed, as indicated by the similar crack growth rate compared with the samples without electropulsing treatment. In addition, a refined microstructure can be achieved after EPT.

I. INTRODUCTION

METALLIC alloys have been extensively used in many aspects of our society, including manufacturing machines for industries, agriculture, automobiles, and aerospace.[1–4] Fatigue failure and fatigue-related phenomena are the main sources of failures in metallic components.[5] It is estimated that more than half of all mechanical failures are originated from fatigue.[6] Fatigue damage in metals begins with initiating microscopically short cracks in regions of stress concentrations followed by the growth of the microcracks into macrocracks and a catastrophic fracture occurs subsequently.[7] In order to avoid severe accidents and huge losses, the fatigued components must be replaced regularly. However, if the microcracks and defects are arrested and/or repaired before they propagate to the point of fracture, the service life of the components can be extended resulting in large economic and environmental benefits.

In the last twenty years, there have been many investigations into crack-healing techniques for fatigued metallic components. First of all, the high-temperature heat treatment technique is the first method that was proposed to heal the surface and internal cracks. Li et al. proposed that the atomic diffusion and recrystallization of subgrain contribute to the healing of the crack by increasing the temperature.[8] More recently, He et al. developed a cyclic phase transformation technique with heat treatment for healing the internal cracks of low-carbon steel.[9] The accelerated healing results from the introduction of dislocation in the matrix. Second, hot plastic deformation or thermal–mechanical coupling has been introduced as a method for healing the crack. The different deformation modes and the temperature of quenching and tempering were investigated.[10] The mechanical properties were optimized with multi-pass at 1150 °C and quenching and tempering treatment. The accelerated crack healing with increasing temperatures, reduction rates, numbers of deformation passes, stain rates, and holding time durations was reported by Yu et al.[11] At last, the controlled high-density electropulsing treatment (EPT) is an effective way for healing the crack.[12] Among the above healing techniques, EPT exhibits great advantages. First of all, the defects and cracks can be detected automatically, due to the current

QING CAI, MIAN ZHOU, EBAD BAGHERPOUR, SEYEDMEHDI HOSSEINI, CHAMINI MENDIS, ISAAC CHANG, and HAMID ASSADI are with the Brunel Centre for Advanced Solidification Technology (BCAST), Brunel University London, Uxbridge UB8 3PH, UK. Contact e-mail: isaac.chang@brunel.ac.uk

concentration of the defects and cracks during the EPT. Second, the microstructure is only changed around the healed crack regions, while the remaining area remains intact. In addition, it is also an energy-efficient technique that high current density input with a duration of less than 0.5 ms.

There are a few investigations on crack healing *via* EPT, and the complete healing of fatigue crack *via* EPT is very challenging. The healing mechanism remains controversial and experimental observation of the EPT phenomenon varies. The first reports of crack healing in 2000 and 2001 confirmed partial healing around the crack tip by EPT.[13,14] The healing of the crack tip region was believed attributed to the low-temperature plasma and the effect of atomic motion. Crack healing by EPT does not require the temperature around the crack tip to reach the melting point of the alloy. In 2004, Yi Zhou *et al.*[12] successfully healed 50 pct of a pre-crack (artificial crack generated by drilling a hole in a sample, then compressing it to make the hole into a crack shape) in medium carbon steel having a length of ~ 0.7 mm. In 2016, Yu *et al.*[15] used the same method to have a ~ 0.6 mm length crack in an austenite stainless steel SUS304. They could achieve a maximum healing length of ~ 0.26 mm after 7 repetitions of EPT at 4.1 kA/mm^2, which is equal to 43 pct of the total crack length. A mixture of columnar and recrystallized grains was found in the partially healed crack region. In other studies in 2012 and 2013, Hosoi *et al.*[16,17] showed a successful crack closure in austenitic stainless steel SUS316 after applying 35 EPT pulses on an ~ 2-mm-long crack. However, from the SEM images, it is obvious that there is not a complete bond between the two sides of the cracks, rather than forming a bridged crack surface. It is attributed to thermal compressive stress and subsequent partial melting induced by electric current discharge. Reduced fatigue crack propagation rate was obtained by Ben *et al.*[18] A large number of melting beads were found inside the open cracks, and there is no obvious metallic bonding between the crack surfaces. According to the mentioned studies, so far, achieving 100 pct healing of the cracks (longer than 1 mm) using the current route of EPT is very challenging. The essential requirements for crack healing remain unclear, and there is a lack of quantitative evaluation of the healing effect of different pulse current densities. Although some simulation works on the healing process through EPT were conducted, the simulation is based on simplified crack geometry for the internal voids/micro-cracks to regular geometry.[19–21] Therefore, a detailed microstructural characterization together with a simulation of the EPT process based on real or approximative fatigue crack geometry is necessary for an in-depth understanding of the crack-healing mechanism.

Motivated by the disparities in understanding, four fatigued samples were prepared with similar crack sizes. Electron backscatter diffraction (EBSD) and micro-CT techniques were used to study the microstructural evolution of fatigue samples with similar crack geometry after EPT with different current densities. For the first time, a simulation of the healing process *via* modeling of the temperature and stress field around the real fatigue crack dimension was carried out to quantitatively understand the healing mechanism. The fatigue crack growth rate was measured on the sample with a completely healed crack. The findings provide not only new insight into crack healing for repairing the fatigued components, but also shed light on the bonding mechanism of partially or highly defective metals subjected to electropulsing treatment.

II. EXPERIMENTS

A commercially available austenite 316L stainless steel with a composition of 10.1 pct Ni–2 pct Mo–16.7 pct Cr–1.11 pct Mn–0.51 pct Si–0.031 pct P–0.022 pct C–0.001 pct S and balance Fe (wt pct) was used in this study. Four samples of austenitic stainless steel were prepared for this study, and they are referred to as Sample A, Sample B, Sample C, and Sample D. These samples were machined with a specific notch near one side with dimensions as shown in Figure 1(a). The tensile fatigue test conditions and final sizes of the fatigue crack are listed in Table I. The samples were ground and polished to prevent surface crack initiation, prior to the fatigue test for generating fatigue cracks. The samples for EBSD were cut from the crack region in each sample, and it was further ground and polished with subsequent vibratory polishing at a frequency of 70 Hz for 3 h.

EPT was carried out by a pulse power generator PS96-16 Bule Wave capacitors (PSTproducts GmbH) with a specifically designed workstation, as shown in Figures 1(b) and (c). The peak-positive current was set between 125 and 250 kA, and the peak negative current was set between -170 kA and -90 kA, as shown in Figure 1(d). The frequency was maintained at 7.5 kHz. The EPT conditions on these four samples are listed in Table II. Samples A, B, and C were electropulse treated with three different peak constant current densities for 50 pulses. In Sample D, the peak-positive current density of 2 kA/mm^2 (same as Sample C) was applied for the first 20 pulses, followed by 30 more pulses with a positive peak current density of 2.15 kA/mm^2. A Jiusion 40 to 1000 × magnification endoscope, digital microscope, is applied for the observation of global microstructure during EPT treatment. A Zeiss SUPERA 35 scanning electron microscope equipped with an electron backscatter diffraction (EBSD) detector was used for microstructural characterization to determine the orientations and grain size in these samples after EPT. Zeiss Xradia 410 Versa X-ray microscope was used for the characterization of the geometry of the fatigue crack before and after EPT.

The tensile fatigue test was conducted at room temperature under axial load. The crack growth rate was tested under a constant stress amplitude of 85 MPa at room temperature, with a stress ratio of 0.54 and a frequency of 15 Hz. The testings were interrupted once the crack length became ~ 1.5 mm. Sample D which was completely healed after EPT was slightly ground and polished, prior to the test of crack growth rate. Three reference samples without EPT were also tested, for the
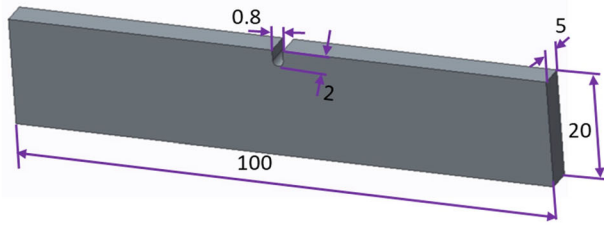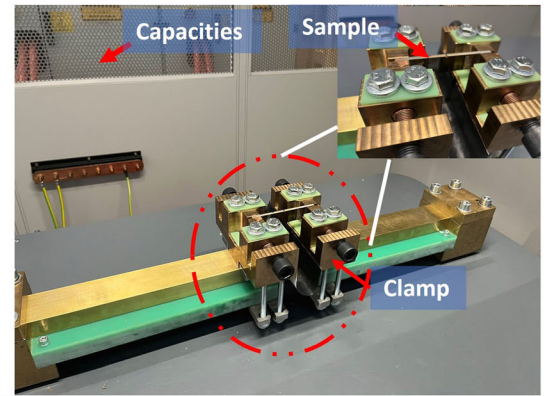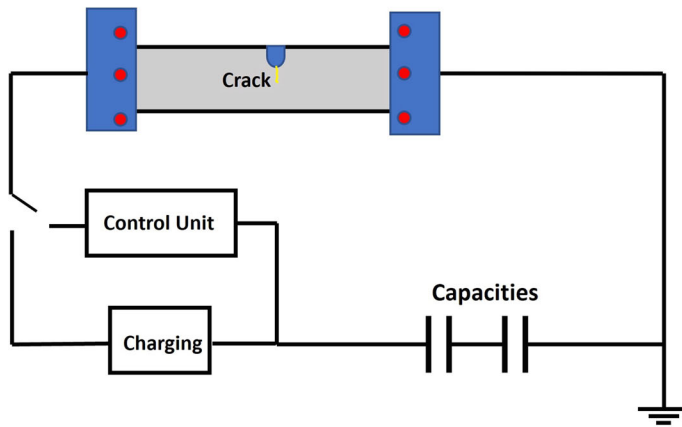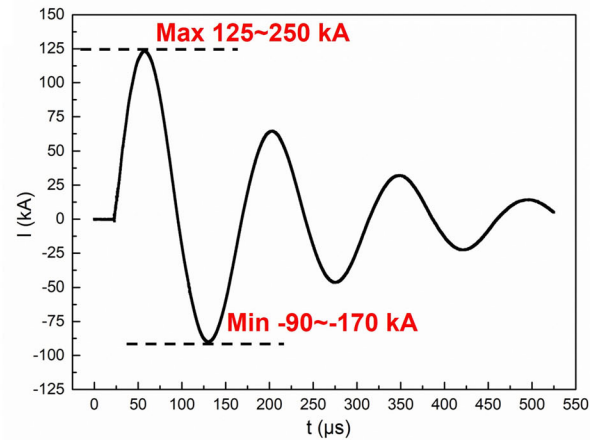
Fig. 1—(*a*) Dimension of the fatigue test sample (unit: mm) (*b*) electropulsing treatment setup (*c*) the schematic diagram (*d*) waveform of electropulsing.

Table I. Fatigue Testing Conditions for Sample A, Sample B, Sample C, and Sample D

Sample Name	Amplitude (KN)	Load (KN)	Frequency (Hz)	Number of Cycles (N)	Crack Width (μm)	Crack length (μm)
A	6	22	15	8.8×10^4	35	1350
B	6	22	15	6.5×10^4	40	1050
C	6	22	15	7.5×10^4	40	1290
D	6	22	15	8.8×10^4	50	1350

Table II. EPT Conditions for Sample A, Sample B, Sample C, and Sample D

Sample Name	EPT Condition	Peak Current density (kA/mm^2) Positive	Negative	Number of Pulses	Pulse Duration (msc)	Frequency (kHz)
A	single step	1.55	-1.16	50	0.5	7.5
B	single step	2.15	-1.65	50	0.5	7.5
C	single step	2.00	-1.45	50	0.5	7.5
D	dual step	2.00 to 2.15	-1.45 to -1.65	$20+30$	0.5	7.5

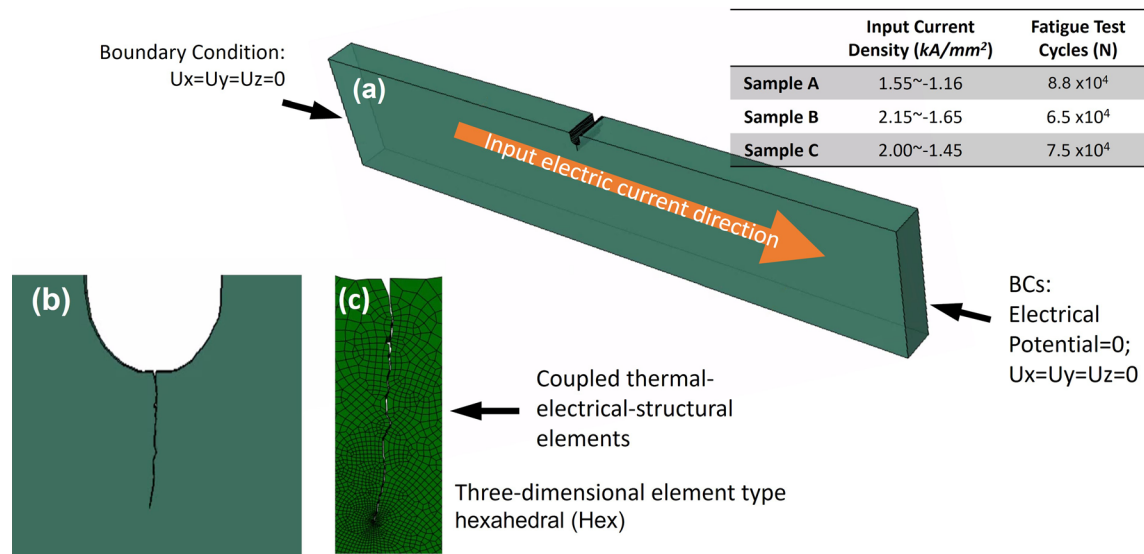|	Input Current Density (kA/mm²)	Fatigue Test Cycles (N)
Sample A	1.55~-1.16	8.8 x10⁴
Sample B	2.15~-1.65	6.5 x10⁴
Sample C	2.00~-1.45	7.5 x10⁴

Fig. 2—(*a*) 3D overview (*b*) fatigue crack (Sample A) close-up view (*c*) finite element mesh around the crack.

comparison of the crack growth rate with Sample D. The three reference samples were also ground and polished, named 316L reference 1, 316L reference 2, and 316L reference 3, respectively. They have the same material and specimen geometry as Sample D. A Jiusion ×40 to ×1000 magnification endoscope, digital microscope, was employed for measuring the crack length during the fatigue test.

A. *FEM Simulation*

The finite element software, Abaqus 2022, was utilized for simulating the temperature and stress distribution around the crack subjected to EPT. The healing mechanism was investigated at the crack tip after one electric pulse. Since a new crack tip is generated after one EPT application, the same healing mechanism is repeated at each EPT until the entire crack is healed after multiple pulses. During the EPT, the electrical current induces Joule heating in the sample, increasing the temperature of the material. The increased temperature gives rise to thermal expansion, which causes plastic deformation in the material. Plastic deformation further increases the temperature of the material. The electrical flow and thermal conduction at the crack tip depend on the contact of the crack surfaces, which is a function of its gap distance. Meanwhile, the temperature field affects the electrical flow and the displacement of the material because of the temperature dependence of the material properties. In effect, the simulation of EPT-healing process requires simultaneous solutions for the electrical potential, temperature, and displacement fields. The fully coupled electro-thermo-mechanical analysis method in Abaqus was, therefore, adopted. The 3D electro-thermo-mechanical model is shown in Figure 2(a). The 'thermal-electrical-structural' element in Abaqus was applied to the mesh, enabling displacement, temperature, and electrical potential degrees of freedom in the model. The Joule heating, heating due to

plastic dissipation, and thermal softening are accounted for in the analysis. The translational displacements are constrained (Ux = Uy = Uz = 0) at both end faces of the sample while other surfaces are unrestrained to represent the clamping boundary conditions in the experiment. The pulse current data used in the experiment were input in the Abaqus model as surface electric current at the left-end face and assumed uniformly distributed at the cross section. The electrical potential was assigned as zero at the right-end face. The skin effect of the 7.5 kHz pulse current was considered negligible for the 5-mm-thick plate of SS316L. The temperature-dependent thermal and physical material parameters adopted in the Abaqus model are summarized in electronic supplementary Table S1. The Johnson cook material model was used for the mechanical analysis, of which parameters are also included in electronic supplementary Table S1.

The crack geometry is simulated in Abaqus based on the SEM images of the crack in each sample. The SEM image is obtained under low magnification and some small features of the crack are not taken into consideration. The definition of mesh size is based on the geometry of the crack. The mesh size is much smaller near the crack tip and much larger near the notch, in order to balance the calculation time and accuracy of the temperature field. The thermal and electrical conductance of the crack was defined as a function of the gap between the contacting crack surfaces. An extremely high value was assigned to thermal conductance $(1 \times 10^{10}$ W/m·K) and electrical conductance $(1 \times 10^{10}$ A/m·V) when the gap clearance was zero; in other words, full heat and electrical conduction were assumed once the crack surfaces closed. The latent heat effect was considered, where the latent heat of the fusion coefficient was defined as 285 kJ/kg, over the temperature ranging from 1350 °C to 1550 °C. The finite element analysis focuses on examining the evolution of thermal gradient and compressive stress as the material

approaches melting temperature at the crack tip, and the solid-to-liquid transition is not explicitly included in the simulation.

III. RESULTS

The applied pulse frequency, pulse duration, and number are the same in these three Samples A–C. The applied peak current densities (positive/negative) for Sample A, Sample B, and Sample C were set to 1.55/ − 1.16 kA/mm^2, 2.15/− 1.65 kA/mm^2, and 2/− 1.45 kA/mm^2, respectively, as listed in Table II. For

simplification, the EPT conditions of these samples were labeled based on positive current density. Figure 3(a) through (c) shows SEM-backscattered images of fatigue cracks present in these three samples before and after EPT. The percentage of healing was calculated by dividing the healed length after EPT by the total length of the crack before EPT. There is no melting observed in Sample A after 50 pulses at the lowest peak current density of 1.55 kA/mm^2, and instead, a reduction in crack width and complete closure of the crack occurs, as shown in Figure 3(a). The melting of the crack as well as the splashing of melting beads in Sample B can be observed in Figure 3(b). Although 49 pct of the
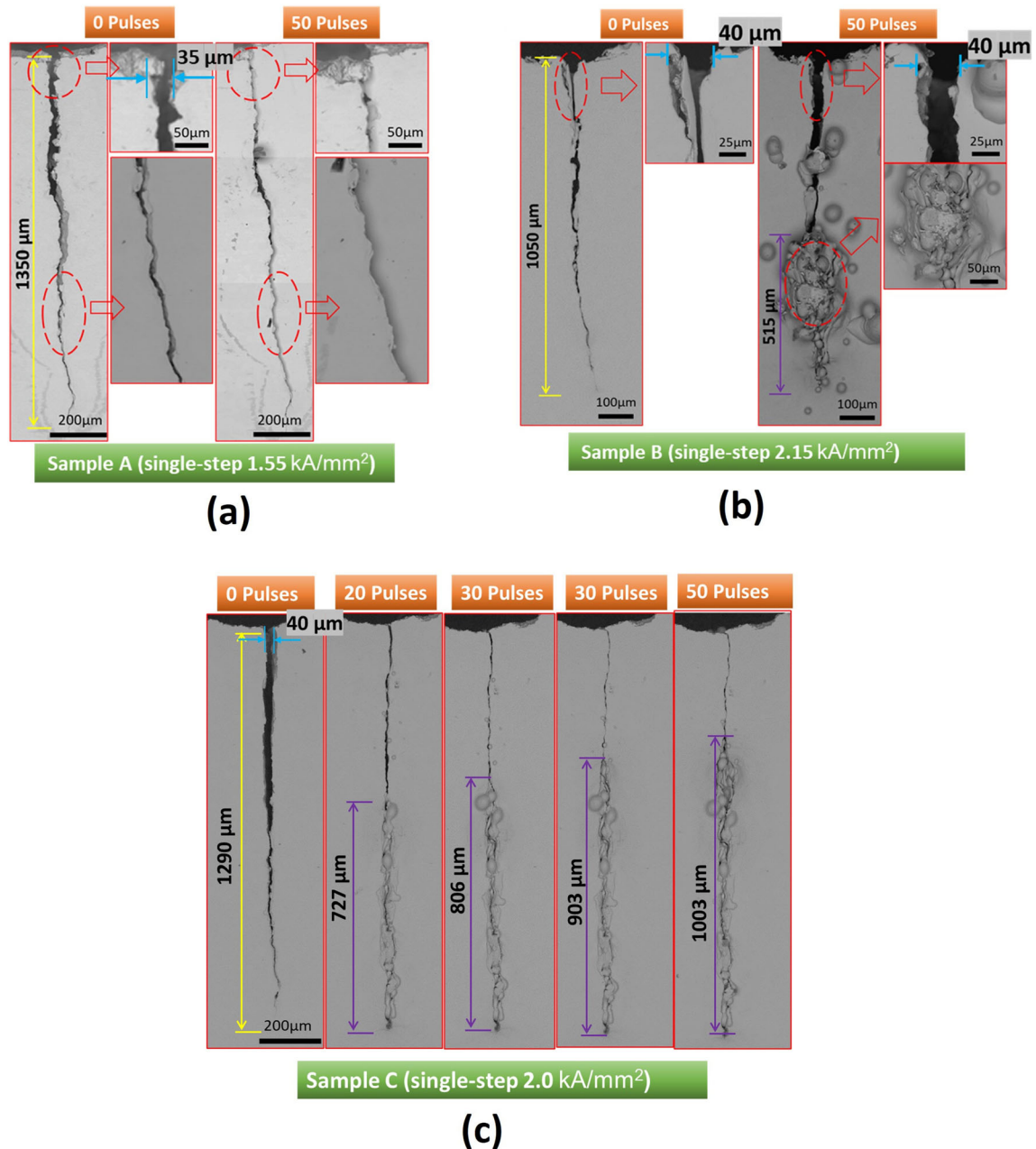

Fig. 3—SEM-backscattered images showing the changes in fatigue crack characteristics before and after EPT as a function of the number of pulses at low (*a*), high (*b*), and medium (*c*) current densities.

crack has been healed in Sample B after 50 pulses at the highest peak current density of 2.15 kA/mm^2, there is very little change in the crack width. This suggests that the highest current density is able to melt the crack; however, the compressive stress for its crack closure is not sufficient. The gradual healing of Sample C is shown in Figure 3(c), indicated by the bonding of the melting beads inside the cracks. In Sample C, 50 pulses at a medium peak current density of 2 kA/mm^2 lead to the complete closure of the crack and healing of 78 pct of the fatigue crack. This observation reveals that the selection of proper current density is necessary for simultaneous crack closure and healing.

Samples A, B, and C are carried out on a certain number of pulses and fixed current density in each sample. Although the selection of the current density under a certain frequency is able to heal and close the crack partly, more healing is very difficult to achieve after a certain number of pulses at a fixed current density. From Figure 3(c), it was evident that after the first 20 pulses, about 56 pct of the crack was healed, while 30 more pulses can only heal 22 pct of the crack. The healing percentage is not linear to the number of pulses under the fixed current density. More pulses at the same current density have limited effects on the healing at a later stage. It is because of the gradual decrease of current density around the crack tip with the increased healing length of the crack. It is essential to increase the current density in order to get more healing percentage. Since the EPT is a dynamic process, the dynamic justification with respect to the healing percentage needs to be further investigated, such as the change of current density. Depending on the size and shape of the crack, more steps may be required (dual processing). Figure 4 shows a schematic diagram of the waveform of a so-called dual EPT processing. As seen, the first step of the EPT consists of n_1 pulses having a maximum peak current intensity of I_{max1}. The first step follows by a further n_2 number of cycles with a higher second maximum peak current intensity of I_{max2}.

Hence, sample D was employed for the investigation of the effect of current density on further healing of the fatigue crack. The crack tip geometry in Sample D is close to Sample C; thus, the starting peak current density of 2 kA/mm^2 was selected. Figure 5(b) shows the microstructure of Sample D after 20 pulses, which is taken by a digital microscope from the notch. The crack was almost closed, while there is no melting near the notch, indicating no healing towards the end of the crack. Correspondingly, the microstructure of the crack from one side in Sample D after 20 pulses is shown in Figure 5(d) and the healing can be observed, accounting for ~ 50 pct of the total length. After 30 more pulses at 2.15 kA/mm^2, the melting beads were observed on the notch which was squeezed from the crack during healing, as shown in Figure 5(c). Meanwhile, the complete healing of the crack is also displayed in Figure 5(e), and the melting can be observed along the crack. Figure 5(f) shows a plot of the healing percentage as a function of the number of pulses for Sample C and Sample D. After 20 pulses, the percentage of healing length is very close to that in Sample C, and after 50 pulses, the complete crack healing can be achieved. The fatigue crack can be completely and effectively healed *via* the adjustment of the current density with the healing percentage.

The Micro-CT was applied for the confirmation of the final healing of internal cracks, as shown in Figure 6. It can be found that the crack was nearly healed to the notched side, as well as squeezed melting beads. There are only a few black dots or wavy black lines inside the healing region from the images after EPT. This indicated some solidification porosities and defects, which are inevitable. Further work such as heat treatment needs to be done for healing the microdefects such as porosity and voids for the great extension of the service life of the metals.

In order to understand the healing mechanism of EPT, the samples after EPT are further cut and polished for EBSD characterization. Figure 7(a) and (b) shows the Inverse Pole Figure (IPF) and Kernel Average Misorientation (KAM) maps of Sample A. The microstructure consists of the fatigue crack, fine dynamic recrystallized grains, and coarse grains. The deformation bands are visible in the KAM map, caused by the compressive stress after EPT, corresponding to the decrease of the crack width. Figure 7(c) shows the secondary SEM image of the crack tip which indicates that the lowest peak current density of 1.55 kA/mm^2 is not able to melt the crack tip. Although crack closure can be observed in Figure 7(a), the crack can still be observed from SEM images under high magnification,
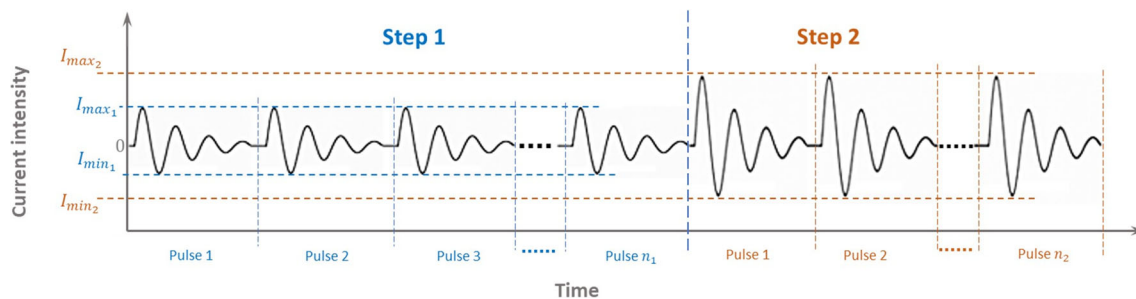

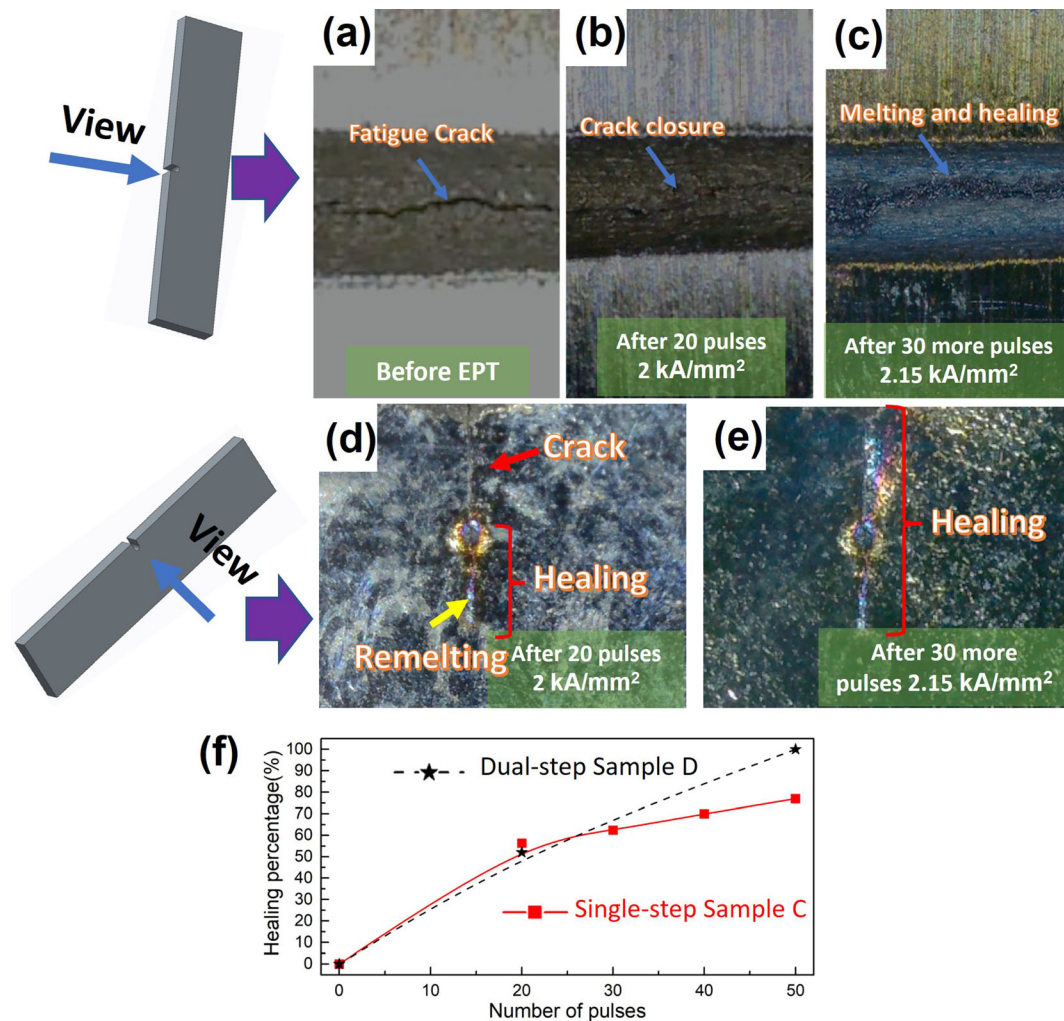Fig. 4—Schematic waveform of dual EPT process.

Fig. 5—Images taken by digital microscope showing the fatigue crack viewing from the notch in Sample D (*a*) before EPT (*b*) after 20 pulses with a current density of 2 kA/mm^2 (*c*) after 30 more pulses with a current density 2.15 kA/mm^2; the fatigue crack viewing from one side of Sample D (*d*) after 20 pulses with current density 2 kA/mm^2 (*e*) after 30 more pulses with current density 2.15 kA/mm^2; (*f*) a plot of healing percentage as a function of the number of pulses for Sample C and Sample D.

as shown in Figure 7(c); therefore, there is no crack healing. A high temperature around the crack tip was achieved as deduced from the fine-recrystallized grains. A similar phenomenon is reported by Rout *et al.*,[22] where fine-recrystallized grains formed during the hot deformation at temperatures over 1000 °C. Furthermore, the medium peak current density of 2 kA/mm^2 used in Sample C contributes to a melting region of 30 to 50 μm width and recrystallized zone as displayed in Figure 7(d). There are several recrystallized fine grains and twinning distributed at grain boundaries or inside the grains, reflecting a high temperature around the molten zone compared with that in Sample A. Figure 7(e) shows severe plastic strain took place in the molten region in Sample C. The defects can be observed at the crack tip from Figure 7(f), which may be caused by the wetting angle between solid/liquid surfaces or solidification porosities. The microstructure after EPT in Sample B is different from Sample C, consisting of remelted fine grains close/at the crack

region, recrystallized grains adjacent to the crack region and unaffected coarse grains in the bulk region, as shown in Figure 7(g). The highest peak current density of 2.15 kA/mm^2 applied in sample B leads to a larger melting zone along the crack length as well as local compressive stresses around the healed crack.[15] The molten region has very fine grains, and there are grains with color gradation surrounding the molten region, which is believed to be the recrystallized region. These two regions are in the heat-affected zone, in which the microstructure is affected by Joule heating.[17] The large residual plastic strain in the heat-affected zone can be observed from the KAM map in Figure 7(h), indicating the plastic deformation during the EPT. The high density of dislocation induced by local plastic deformation combined with high temperature triggers the recrystallization of the fine subgrains, which might be attributed to dynamic recrystallization behavior.[23] In the meantime, the molten region with 30 to 80 μm width, solidified accompanied by rapid heat dissipation
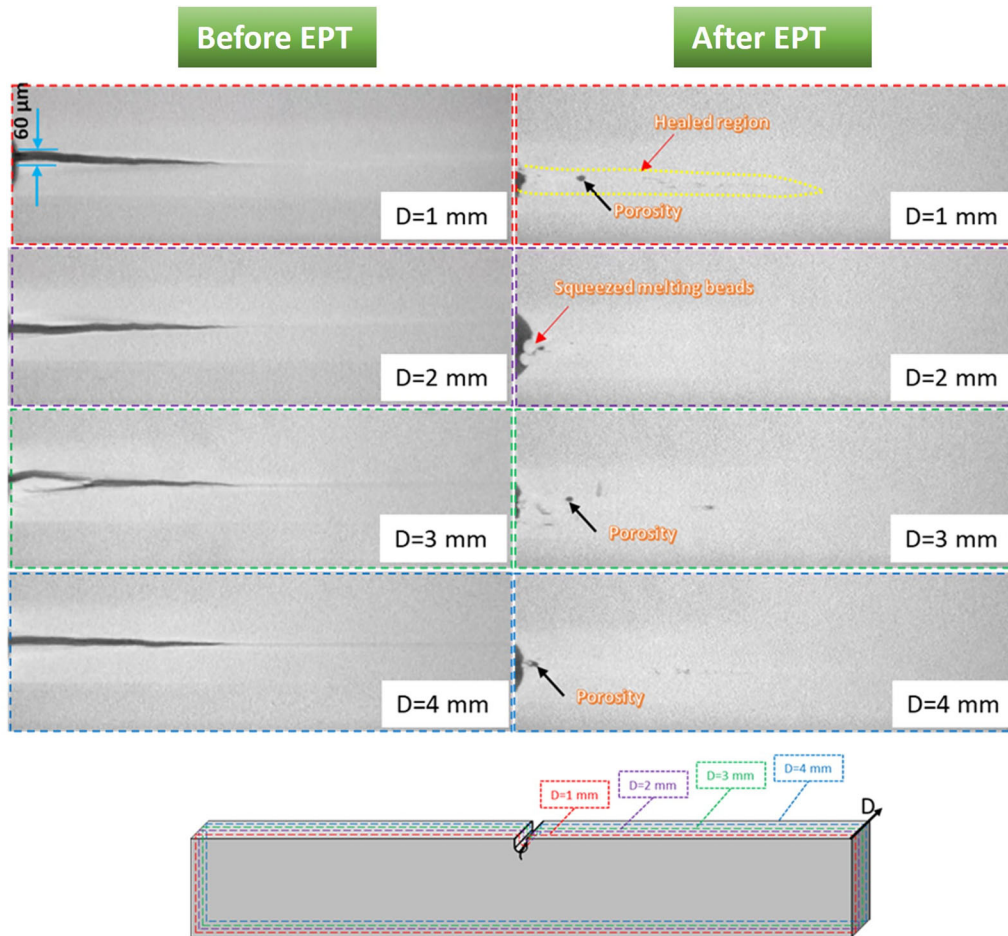
Fig. 6—Images of slides obtained from the Micro-CT at the different thicknesses of Sample D before and after EPT.

as well as compressive stress. Consequently, large plastic strain and fine grain size are achieved after EPT. There are some solidification porosities in the healing region shown in Figure 7(i), which are typical defects associated with solidification. In addition, the distribution of grain size of the remelting region in sample C and sample B is shown in Figure 7(j). The average grain size of melting region in sample C is smaller than that in sample B. It may result from the higher temperature gradient around the crack tip in sample B, and the cooling rate during solidification is lower.

Figure 8(a) and (d) shows the IPF maps of the region away from the crack tip in Sample C and Sample B after EPT, respectively. The microstructure is similar to the crack tips, having a fine remelting and recrystallization region. The equiaxed grains are displayed in the remelting region. In the recrystallization region, the coarse grains have a color gradient, which indicates large plastic deformation.[24] It coincides with the KAM maps in Figure 8(b) and (e). In addition, there are subgrains and twinnings inside the large grains. The healing is a non-isothermal process with a very short time span. Thus, incomplete recrystallization might occur, leading to some fine subgrains inside the coarse grains.[25] The twinings may result from mechanical

deformation or/and an annealing effect during healing.[26,27] The SEM secondary electron images in Figures 8(c) and (f) show the melting and bonding in the corresponding healed regions. The porosities were also found, which are caused by the solidification. The average grain size distribution of remelting region in sample C and sample B is shown in Figure 8(g). It can be found that the grain size in sample C is finer than that in sample B, which coincides with the results in Figure 7(j).

Figure 9 compares fatigue crack growth rates of the complete healing sample (Sample D) and three reference samples without EPT. The curves of da/dN versus ΔK (stress intensity factor) in these four samples show a linear relationship following Paris' law (da/dN = $C(\Delta K)^m$),[28] and they are very close. Therefore, the fatigue resistance of Sample D and the three reference samples (without EPT) are close to each other. Crack healing *via* EPT is effective for improving the fatigue life of the components.

The fracture surface and cross section near the fracture surface of the sample without EPT are shown in Figure 10(a) and (b), respectively. The numerous striation lines as well as tear ridges were found in the fracture surface shown in Figure 10(a), indicating the
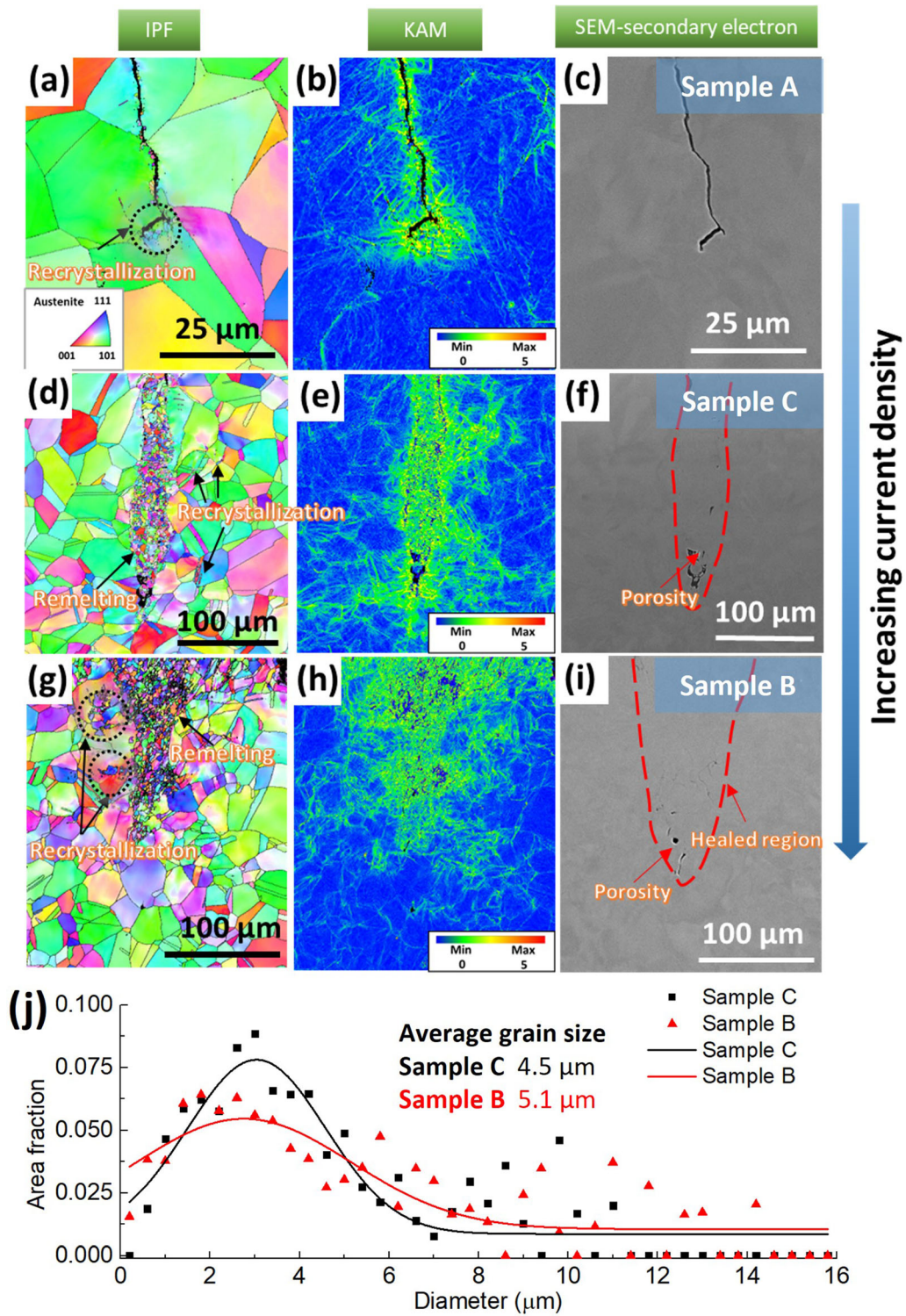
Fig. 7—(*a*, *d*, *g*) Inverse Pole Figure (IPF) maps (*b*, *e*, *h*) the Kernel Average Misorientation (KAM) maps (*c*, *f*, *i*) SEM secondary electron images of the crack tip after EPT from Sample A, Sample C, and Sample B, respectively, (*j*) grain size distribution of the remelting region in Sample C and Sample B.

crack propagation direction. Combined with the microstructure in Figure 10(b), the fatigue crack in the sample without EPT is a transgranular mode. However, Figure 10(c) shows the ductile fracture surface with many dimples in Sample D after EPT. The fracture region in Sample D after EPT results from the nucleation, growth, and coalescence of the voids. The size of the dimples is 1 to 5 μm, which is very close to the grain size in the melting region as shown in Figure 8(a). It can be induced that the crack propagation is along the
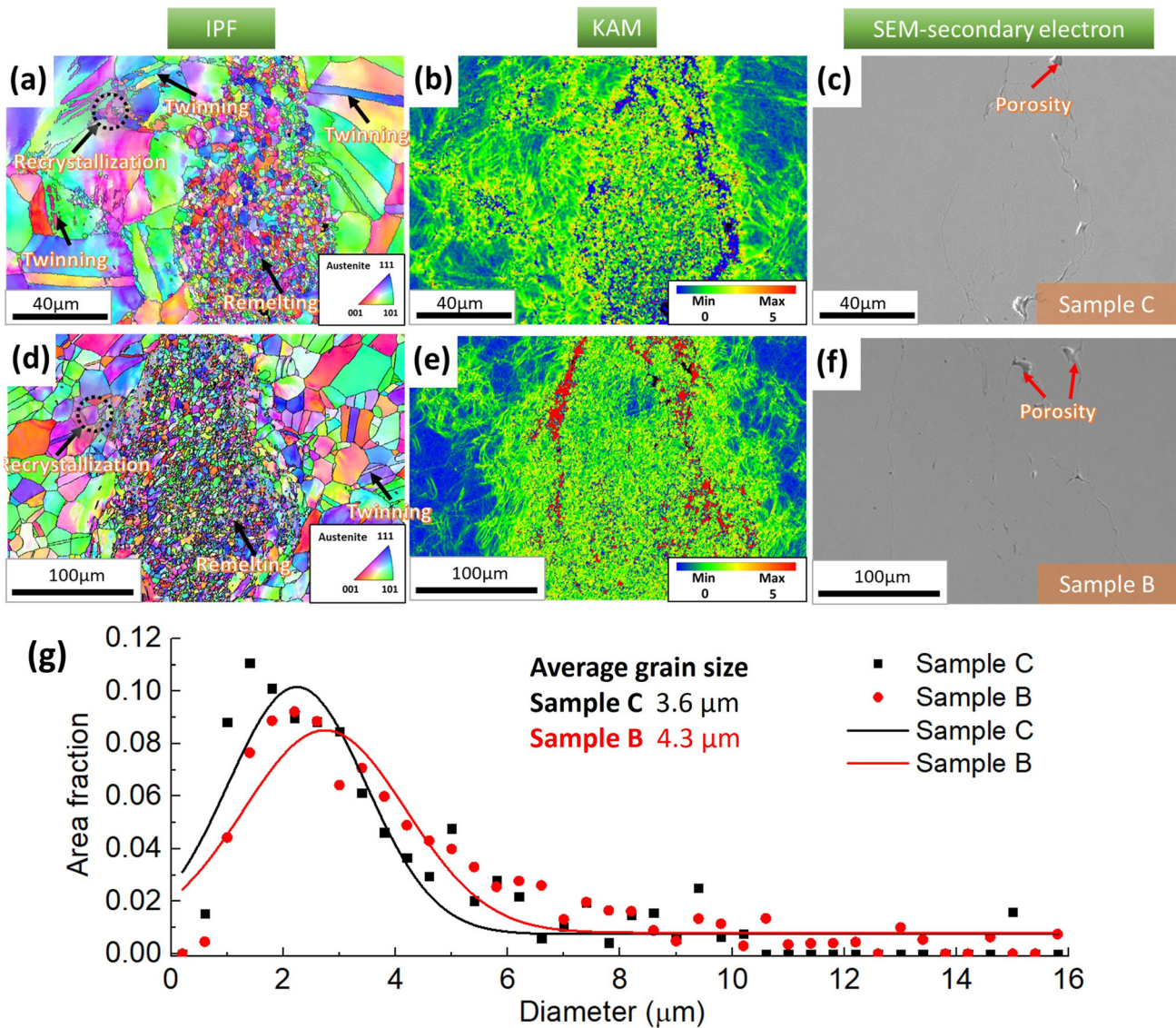
Fig. 8—(*a, d*) IPF maps (*b, e*) KAM maps (*c, f*) SEM secondary electron images of the region away from the crack tip after EPT from Sample C and Sample B, respectively, (*g*) grain size distribution of the remelting region in Sample C and Sample B.

healing region. It is further confirmed by the microstructure in Figure 10(d) which shows the separation of the crack surface in the remelting region. A similar fracture phenomenon after EPT was reported by Ben *et al.*[18] The electropulsing treatment on fatigue cracks can provide strong metallic bonding between crack surfaces after healing.

IV. DISCUSSION

Interestingly, the large current density is necessary for crack healing, which is able to melt the crack region. However, the crack closure cannot be observed in Sample B. The electro-thermo-mechanical simulation was carried out using the Abaqus-based FEM model to facilitate a better understanding of the crack-healing mechanism. The complexity of the healing process involves liquid-to-solid state transformation as well as the change of the crack length with the number of pulses; thus, it is unrealistic for the simulation of the whole process. However, the selection of the current density in the first pulse is very important. Too much high current density will cause damage to the sample, such as the melting of the sample after one pulse or a large molten hole in the crack tip.[13] In addition, once the crack tip was healed and a new crack tip was generated. Further healing occurs on the new crack tip, caused by the concentration of current on the new crack tip. For simplification, the stress and temperature field after the first pulse of EPT were simulated. The simulation results are discussed in view of correlations with the experimental observations; thereby, possible criteria for crack healing are assessed. Based on these criteria, correlations between successful crack healing and critical parameters of the EPT process are

evaluated. When the pulse with a given current density is applied to the fatigued sample, the geometric singularity causes a large electric current density concentration localized at the crack tip, thus, where the temperature rises to the highest and the maximum temperature gradient occurs. Figure 11(a) shows the temperature distribution around the crack tip for the three samples. The temperature development against the distance from the crack tip is plotted in Figure 11(b). The crack tips in Sample B and C have a region with a temperature over the melting point, and Sample B experiences the largest
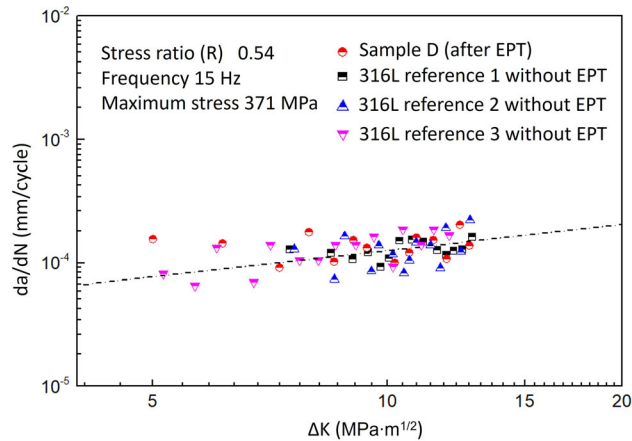
Fig. 9—Fatigue crack growth rate as a function of stress intensity factor range of Sample D and three reference samples.

heat-affected zone and melting zone. There is no melting in Sample A and the maximum temperature on its crack tip is below 1400 °C. These coincide with the experiment results. The thermal expansion in the vicinity of the crack tip is restrained by its cooler surrounding region, resulting in a compressive stress field at the crack tip. Figure 11(c) shows the temporal development of compressive stresses at the crack tip. The lowest maximum compressive stress (< 200 MPa) was obtained in Sample B, which is much less than its yield strength at room temperature.[29] Thus, no crack closure can be observed in Sample B. This can be attributed to its large heating zone, where excessive material softening around the crack tip could not provide sufficient thermal restraining. Despite the highest maximum compressive stress (~ 600 MPa), Sample A does not exhibit crack healing in the experiment because of no molten zone. In the experiment, crack healing was observed from Sample C, in which both a melting zone and high thermal compressive stresses were obtained at the crack tip in the Abaqus model.

Based on the simulation and experimental results, the fatigue crack evolutions in the current work are summarized in Figure 12. At a certain level of current density, the final crack evolution after EPT can be divided into three types. First, from the example in Figure 12(a), the current density is not high enough and the temperature of the crack tip is below melting temperature. The recrystallization on the crack tip and thin layer of the crack surface together with crack closure can be observed after a few pulses. Second, the
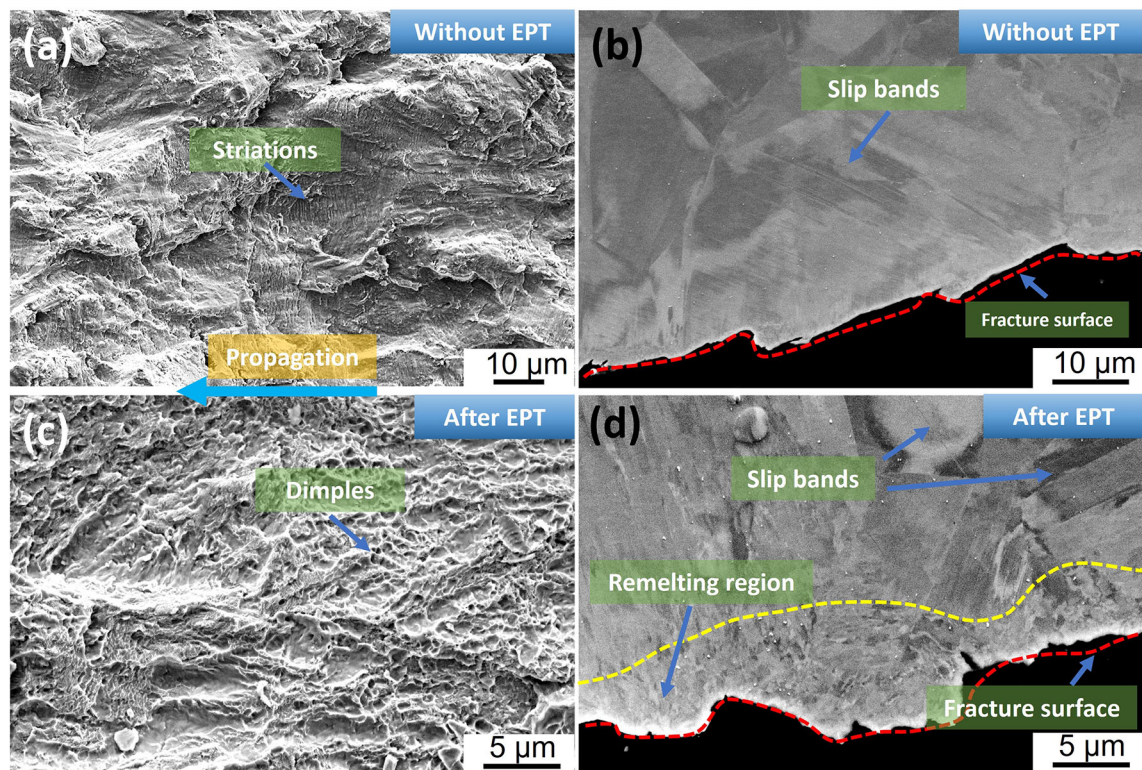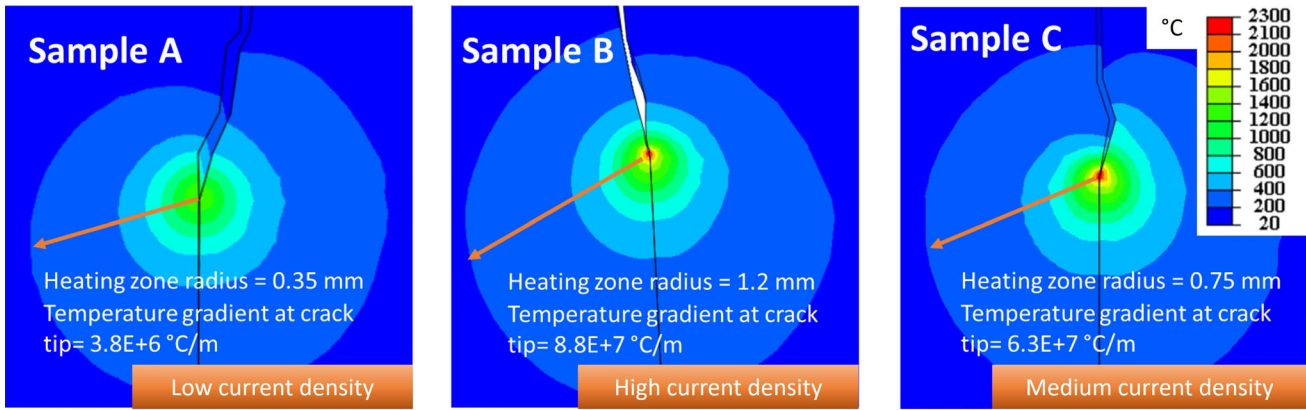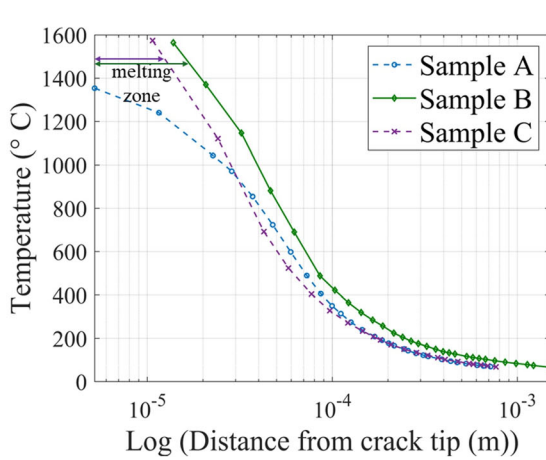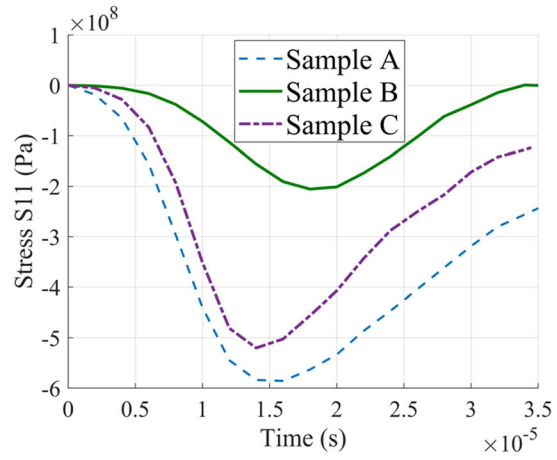

Fig. 10—Fracture surface of the reference sample without EPT (*a*) after EPT in Sample D (*c*); cross section near fracture surface of the reference sample without EPT (*b*) after EPT in Sample D (*d*).

Fig. 11—(a) Temperature field of Sample A, Sample B, and Sample C after the first pulse of EPT (b) temperature distribution against the distance from the crack tip (c) the development of compressive stress at the crack tip.

large melting region is triggered by the high current density, while there is not enough compression stress to squeeze the melt and close the crack. Thus, the melt is gradually accumulated on the crack tip. The further build-up of the melting beads will not be able to fill the gap between the cracks, due to the large width of the crack away from the tip. Instead, the melting beads will split away as shown in Figure 12(b). At last, the right melting zone and compressive stress are able to squeeze the melt and lead to the bonding between the two surfaces of the crack. The heating affecting zone near the two sides of the crack surface is favorable for bonding. With the increasing healing percentage reflected by the reduced length of the crack, the concentration of current density on the formed crack tip is not able to provide healing. Thus, higher current density *via* increased input energy of each pulse is needed for further healing of the crack, which is displayed in Figure 12(c).

Above all, there are two main criteria for crack healing *via* EPT. First is the essential melting around the crack. The average temperature rise after EPT can be calculated by equation:[30]

$$\Delta T = j^2 t_p \left(C_p d\sigma \right)^{-1}, \qquad [1]$$

where σ is electrical conductivity, d is the density of the material, C_p is specific heat, t_p pulse duration, and j current density. From the equation, it can be found that it is more difficult to heal the alloys with higher electrical conductivity. Hence, a lower frequency or high current density is needed for melting the crack tip, in order to heal it. The second criterion is the temperature gradient around the crack tip, which requires maximum compressive stress over its room-temperature yield strength and prevents softening around the crack tip region, at the same time. It has a close relationship to the geometry of the crack tip, and in another word, the different levels of current density may lead to a different temperature field on the different crack tips. The simulation is a very feasible way for the selection of the optimized current density and pulse duration for crack healing. The current work is based on a regular fatigue sample with a certain length of crack. When it comes to real fatigued components, the design of the EPT clamp as well as the
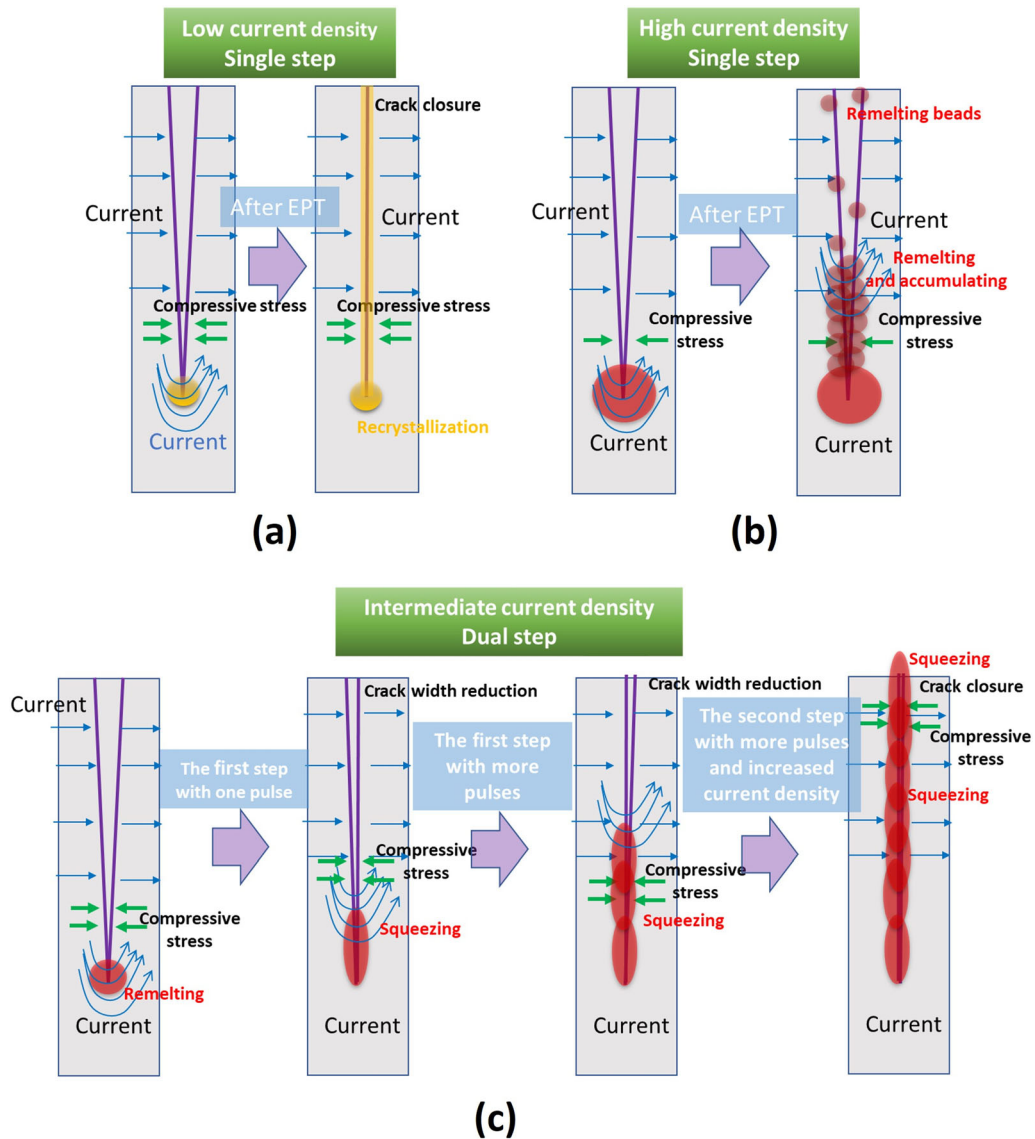
Fig. 12—Schematic illustration of fatigue crack evolution after EPT (*a*) low current density with a single step (*b*) high current density with a single step (*c*) intermediate current density with dual step.

placement of electrodes is essential for the flexibility of crack healing. At last, the solidification porosity of the healed crack is inevitable, and it is harmful to the mechanical performance of the alloys. Future work on the healing of internal porosities is a potential way for the great extension of the service life of metals.

At last, the effects of EPT on the microstructure of austenite stainless steel were studied. Figure 13(a) shows the IPF map of the sample without EPT. Figure 13(b) shows IPF map of the region away from the healed crack in Sample C after EPT for 50 pulses at a current density of 2 kA/mm^2. From Figure 13(b), it can be found that the microstructure consists of a mixture of fine-recrystallized grains and relatively coarse grains. The grain size distribution of the sample without EPT and after EPT is shown in Figure 13(c). The EPT is able to affect the microstructure of austenite stainless steel,

which is indicated by a finer grain size. The misorientation angle distribution is shown in Figure 13(d). There is almost no difference between the two samples, and both of the samples have little low-angle grain boundaries (LAGBs), which indicates low residual stress before and after EPT.[31] There are mainly two parts affecting the microstructure of the samples after EPT, which are thermal effect and athermal effect.[31,32] The athermal effect is also called the electron wind force. From Eq. [1], it can be calculated that the average temperature rise (thermal effect) is about 206 °C after one pulse. The increased temperature is not high enough to cause phase transformation after one pulse. In addition, due to the short duration and fast heat dissipation between the sample and copper clamp, the Joule heating effect on the recrystallization of the sample with multi-pulses is very limited. After 50 pulses, the
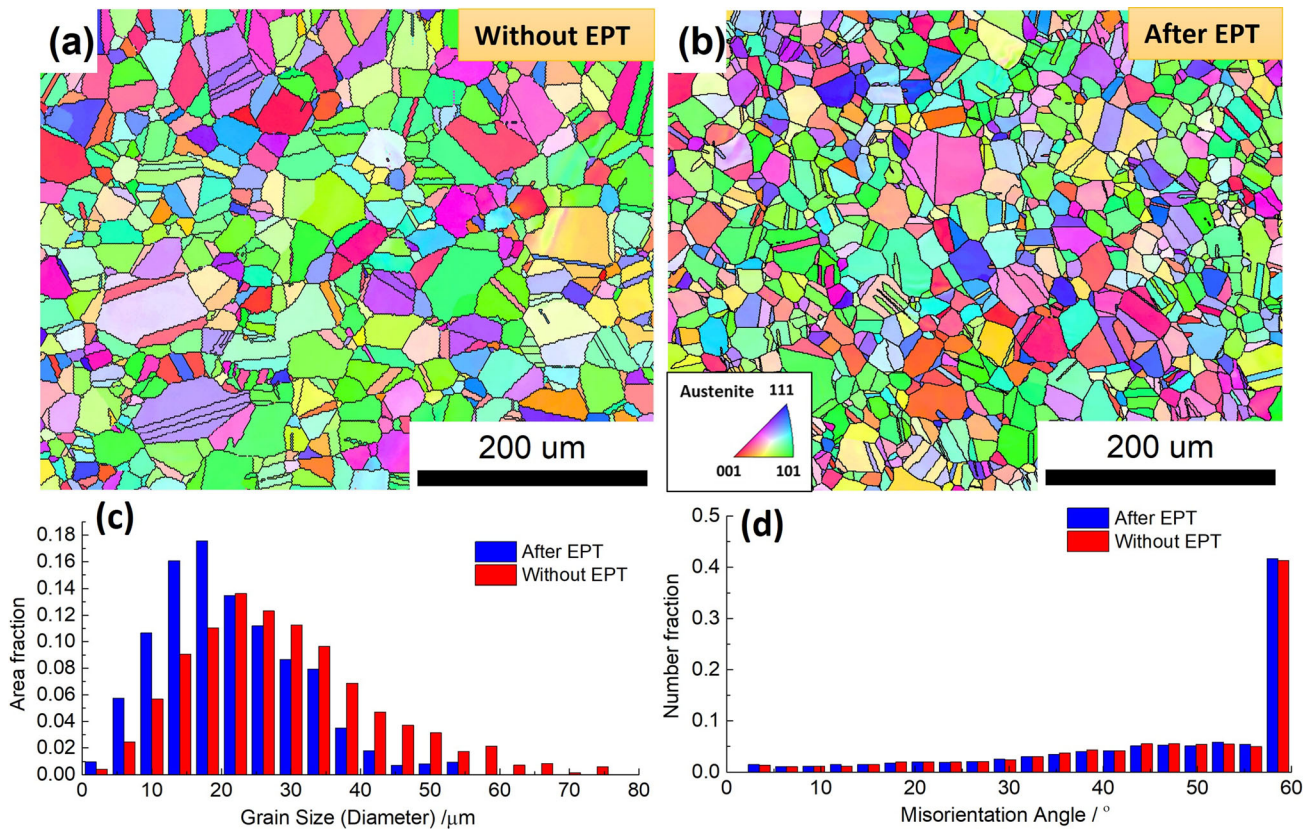
Fig. 13—(a) IPF map of the sample without EPT (b) IPF map of the region away from the healed crack in Sample C after EPT for 50 pulses at a current density of 2 kA/mm² (c) grain size distributions (d) misorientation angle distributions.

temperature of the samples is measured to be ~ 180 °C, considering the cooling time including capacity charging time (~ 10 seconds) and the interval between each pulse (~ 25 seconds). The total time of EPT applied on the sample after 50 pulses is about 25 ms. Here, the athermal effect plays an important role in the refinement of the grains. First, it is reported that EPT is able to decrease the energy barrier of recrystallization, and the critical temperature of recrystallization can be reduced.[33] Second, the mobility of dislocations can be enhanced during EPT.[31,32] The accumulation of dislocations at grain boundaries leads to the formation of subgrains. Finally, recrystallization occurred. The refined grain size is favorable for the high strength of the sample.

V. CONCLUSION

In summary, the finite element analysis and EBSD results revealed that achieving both melting and sufficient compressive stress at the crack tip is essential for successful crack healing. The forming of a localized melting zone at the crack tip is able to create localized healing and sufficient thermal compressive stress. Hot compressive deformation further enables a metallurgical bonding between the crack surfaces that are brought into contact via thermal expansion. The dual-step EPT is effective for the complete healing of the fatigue crack.

The complete healing of the fatigue crack in 316L stainless steel can be achieved with 20 pulses at 2 kA/mm² and the following 30 pulses at 2.15 kA/mm². Therefore, the process parameters of the EPT should be selected to supply the appropriate temperature gradient and compressive stress with respect to the healing percentage. The metallic bonding via EPT is very effective to extend the fatigue life of metallic components. The refined microstructure can be achieved after EPT, which is favorable for mechanical performance.

CONFLICT OF INTEREST

The authors state that there is no conflict of interest.

DATA AVAILABILITY

OPEN ACCESS

SUPPLEMENTARY INFORMATION

REFERENCES

1. M. Peters, J. Kumpfert, C.H. Ward, and C. Leyens: *Adv. Eng. Mater.*, 2003, 5, vol. 5.
2. A. Heinz, A. Haszler, C. Keidel, S. Moldenhauer, R. Benedictus, and W.S. Miller: *Mater. Sci. Eng. A*, 2000, vol. 280, pp. 102–07.
3. N.R. Baddoo: *J. Constr. Steel Res.*, 2008, vol. 64, pp. 1199–1206.
4. D. Raabe, C.C. Tasan, and E.A. Olivetti: *Nature*, 2019, vol. 575, pp. 64–74.
5. S.M.O.O. Tavares and P.M.S.T.S.T. de Castro: *Fatigue Fract. Eng. Mater. Struct.*, 2017, vol. 40, pp. 1510–29.
6. R.I. Stephens, A. Fatemi, R.R. Stephens, and H.O. Fuchs: *Metal Fatigue in Engineering (1980)*, 1981.
7. P. Peralta and C. Laird: *Physical Metallurgy*, vol. 1, 5th ed., Elsevier, Amsterdam, 2014, pp. 1765–80.
8. X. Li, C. Dong, H. Chen, and W. Chu: *Jinshu Xuebao/Acta Metall. Sin.*, 2001, vol. 37, pp. 1093–96.
9. M. He, Z. Zhentai, F. Shi, D. Guo, and J. Yu: *Mater. Sci. Eng. A*, 2020, vol. 772A, p. 138712.
10. Y. Qiu, R. Xin, J. Luo, and Q. Ma: *Mater. Sci. Eng. A*, 2020, vol. 778A, p. 139073.
11. H. Yu, X. Liu, X. Li, and A. Godbole: *Metall. Mater. Trans. A*, 2014, vol. 45A, pp. 1001–09.
12. Y. Zhou, J. Guo, M. Gao, and G. He: *Mater. Lett.*, 2004, vol. 58, pp. 1732–36.
13. Z. Yizhou, Z. You, H. Guanhu, and Z. Benlian: *J. Mater. Res.*, 2001, vol. 16, pp. 17–9.
14. Y. Zhou, R. Qin, S. Xiao, G. He, and B. Zhou: *J. Mater. Res.*, 2000, vol. 15, pp. 1056–061.
15. T. Yu, D. Deng, G. Wang, and H. Zhang: *J. Clean. Prod.*, 2016, vol. 113, pp. 989–94.
16. A. Hosoi, T. Kishi, and Y. Ju: *Materials (Basel)*, 2013, vol. 6, pp. 4213–25.
17. A. Hosoi, T. Nagahama, and Y. Ju: *Mater. Sci. Eng. A*, 2012, vol. 533, pp. 38–42.
18. D. Ben, H. Yang, Y. Ma, Q. Wang, Y. Tian, P. Zhang, Q. Duan, and Z. Zhang: *Adv. Eng. Mater.*, 2019, vol. 21, p. 1801345.
19. X. Lai, Z. Yi, and W. Bo: *AIP Conf. Proc.*, https://doi.org/10.1063/1.4979766.
20. H. Song, Z.J. Wang, X.D. He, and J. Duan: *Sci. Rep.*, 2017, vol. 7, pp. 1–11.
21. X. Ren, Z. Wang, X. Fang, H. Song, and J. Duan: *Mater. Des.*, 2020, vol. 188, p. 108428.
22. M. Rout, R. Ranjan, S.K. Pal, and S.B. Singh: *Mater. Sci. Eng. A*, 2018, vol. 711, pp. 378–88.
23. H. Mirzadeh, M.H. Parsa, and D. Ohadi: *Mater. Sci. Eng. A*, 2013, vol. 569, pp. 54–60.
24. R. Yoda, T. Yokomaku, and N. Tsuji: *Mater. Charact.*, 2010, vol. 61, pp. 913–22.
25. M.S. Ghazani and B. Eghbali: *Mater. Sci. Eng. A*, 2018, vol. 730, pp. 380–90.
26. C.L. Yang, H.J. Yang, Z.F.J. Zhang, and Z.F.J. Zhang: *Scr. Mater.*, 2018, vol. 147, pp. 88–92.
27. D. Jorge-Badiola, A. Iza-Mendia, and I. Gutiérrez: *Mater. Sci. Eng. A*, 2005, vol. 394, pp. 445–54.
28. W.A.P. Paris, M. Gomez, P.C. Paris, M.P. Gomez, and W.E.P. Anderson: *Trend Eng.*, 1961, vol. 13, pp. 9–14.
29. J.B. Vogt, J. Foct, C. Regnard, G. Robert, and J. Dhers: *Metall. Trans. A*, 1991, vol. 22A, pp. 2385–392.
30. H. Conrad and A.F. Sprecher: *Dislocations in Solids*, Elsevier, Amsterdam, 1989.
31. Y. Dong, D. Ben, H. Yang, X. Shao, X. Wang, and Z. Zhang: *Adv. Eng. Mater.* https://doi.org/10.1002/adem.202101623.
32. S.J. Kim, S.D. Kim, D. Yoo, J. Lee, Y. Rhyim, and D. Kim: *Metall. Mater. Trans. A*, 2016, vol. 47A, pp. 6368–73.
33. X.L. Wang, J.D. Guo, Y.M. Wang, X.Y. Wu, and B.Q. Wang: *Appl. Phys. Lett.*, 2006, vol. 89, p. 061910.
34. Y. Ma, M. Dong, J. Geng, W. Xin, L. Meng, H. Yang, and Z. Zhang: *AIP Adv.* https://doi.org/10.1063/5.0106776.